Gradient Descent Optimization Based Parameter Identification for FCS-MPC Control of *LCL*-Type Grid Connected Converter

Bo Long, *Member, IEEE*, Zilin Zhu, Wandi Yang, Kil To Chong, José Rodríguez, *Fellow, IEEE*, and Josep M. Guerrero, *Fellow, IEEE*

***Abstract*—Aging and temperature changes in the passive components of an *LCL*-filter grid connected converter system (GCCs) may lead to parameter uncertainties, which can in turn influence its modeling accuracy for finite-control-set model predictive control (FCS-MPC). The presence of model errors will change the resonance point and deteriorate the power quality of the grid current, in turn degrading the active damping performance. In this situation, there is a serious possibility that the GCCs may malfunction and automatically disconnect from the grid, causing great challenges to the system stability. To solve this problem, first, prediction error analysis in FCS-MPC due to the model parameter errors is presented. Second, to achieve high accuracy and fast filter parameter estimation in utility, an adaptive online parameter identification method based on gradient descent optimization (GDO) has been proposed. Finally, to further reduce the searching time needed by the optimal iteration step, a variable iteration step searching method based on the root-mean-square-prop (RMSprop) GDO method is proposed. Experimental studies of an *LCL*-GCCs prototype in the laboratory have been conducted to validate the effectiveness of the proposed method.**

***Index Terms*—Gradient descent optimization, model predictive control, parameter identification, predictive control.**

Manuscript received November 1, 2020; revised December 29, 2020 and February 4, 2021; accepted February 21, 2021. Date of publication March 10, 2021; date of current version December 6, 2021. This work was supported in part by the Fundamental Research Funds for the Central Universities of China under Grant ZYGX2019J033, in part by the Key R&D Plan of Science and Technology Department of Sichuan Province under Grant 20ZDYF2816, in part by the State Key Laboratory of Control and Simulation of Power System Generation Equipment, China under Grant SKLD20M11, in part by the Tsinghua University, China, and in part by the VELUX FOUNDATIONS under the VILLUM Investigator Grant Center for Research on Microgrids under Award 25920. *(Corresponding author: Bo Long.)*

Bo Long, Zilin Zhu, and Wandi Yang are with the School of Mechanical and Electrical Engineering, University of Electronic Science and Technology of China, Chengdu 611731, China (e-mail: longbouestc1980@126.com; shenmodda@qq.com; wandiyang004@163.com).

Kil To Chong is with the Department of Electronics and Information Engineering, Jeonbuk National University, Jeonju 54896, South Korea (e-mail: kitchong@jbnu.ac.kr).

José Rodríguez is with the Faculty of Engineering, Universidad Andres Bello, Santiago 8370146, Chile (e-mail: jose.rodriguez@unab.cl).

Josep M. Guerrero is with the Department of Energy Technology, Aalborg University, DK-9220 Aalborg, Denmark (e-mail: joz@et.aau.dk).

Color versions of one or more figures in this article are available at https://doi.org/10.1109/TIE.2021.3063867.

Digital Object Identifier 10.1109/TIE.2021.3063867

I. Introduction

OVER the last decade, the development of renewable energy distributed generation systems (RE-DPGS) has attracted substantial interest because of the global energy crisis, and grid connected converter system (GCCs) have been widely used [1]. The GCCs is a key part of connecting RE-DPGS to the power grid, and its robust performance directly affects the grid stability, so it is imperative to conduct research on the advanced control strategy of the power converter in high penetration RE-DPGS [2].

To achieve great performance of the GCCs, besides the classical linear control strategies [3], [4], a large number of nonlinear control methods, e.g., sliding mode control [5], passivity-based control [6], fuzzy control [7], neural network control [8]–[10], H_∞ robust control [11], and so on, have been proposed. As one of the nonlinear control schemes, model predictive control (MPC) has also attracted much attention in recent years, since the problem of computational burden has been preliminary solved by sphere decoding [12]–[15].

Generally, finite-control-set MPC (FCS-MPC) has several advantages, such as a fast dynamic response, simple implementation, and straightforward handling of nonlinearities and flexible control objective constraints [16]. This enables the simultaneous control of various physical variables in the system, such as voltage [17], current [18], torque and flux, switching frequency [19], etc. Due to the high degree of flexibility in determining the cost function, FCS-MPC has been widely used in power electronics [20], [21]. However, during normal operation, because of the aging phenomena and the temperature increase caused by system overload and magnetic coupling, parameters of the filter inductance and capacitance may deviate from their nominal values, which may lead to the model parameter errors in FCS-MPC [22]. As a result, the power quality of the grid current may substantially deteriorate and the GCCs may malfunction, thus endanger the system stability [23]–[25].

In recent years, due to the fast development of MPC in power converters, solutions for parameter disturbance have attracted substantial interest from many scholars. In [26] and [27], the effect of parameter mismatch on MPC control has been analyzed.

0278-0046 © 2021 IEEE. Personal use is permitted, but republication/redistribution requires IEEE permission.
See https://www.ieee.org/publications/rights/index.html for more information.

Authorized licensed use limited to: Universidad Andres Bello. Downloaded on June 25,2024 at 19:34:06 UTC from IEEE Xplore. Restrictions apply.

Generally, there are two common methods used for parameter mismatch in the FC-MPC system.

1) Parameter mismatch is seen as a disturbance in the system. In [28], an adaptive reference model predictive control is proposed for an *LC*-filter inverter with resistive load, wherein the control constructs virtual references generated by a flexibly-modeled virtual multiple-input-multiple-output system to improve the system robustness. In addition, an adaptive robust predictive current control is proposed for *LCL*-GCCs that exhibits zero steady-state current error, and the error correction is achieved by an adaptive strategy that works in parallel with the deadbeat algorithm [29]. A more common solution is that the parameter mismatch of *L*-GCCs is treated as a disturbance, and in this solution, the robustness of the control system is enhanced by establishing a disturbance estimator to compensate for the system disturbance [30], [31]. In [32], a novel model-free predictive current control approach without filter parameter for *L*-GCCs is proposed, which only measures the input currents and calculates their differences under different switching states. Moreover, a model-free method is also used in the control of a multilevel converter and PMSM [33], [34].
2) Parameter identification methods are applied in power electronics for uncertain parameters. Kwak *et al.* [35] proposed an adaptive online parameter identification technique, which is based on the least-square-estimation method for *L*-type active front ends to overcome model mismatch and parameter uncertainties. In [36], an online inductance estimation method is proposed for the virtual-flux based direct power control of an ac–dc converter. In [37], a real-time identification method for the *LCL*-filter in GCCs is presented, which is realized by a recursive estimation algorithm. In addition, qualitative observers have established practical guidelines for adjusting the modeled inductance to reduce the possible mismatches [38], [39].

Currently, the *LCL*-filter has been widely used in GCCs due to its better filtering effect and smaller size. However, the existing research on parameter identification is mostly based on *L*-type GCCs, which are substantially simpler. For multiple parameter estimation, such as three-phase *LCL*-GCCs, there are totally nine filter parameters to be estimated. However, not many studies have been found examining multiple parameter estimation in one system. In addition, fast and high accuracy filter parameter estimation needs to be fully investigated for FCS-MPC controlled *LCL*-GCCs. Motivated by the unsolved issues, in this article, an root-mean-square-prop (RMSprop) gradient descent optimization (GDO) gradient descent method is used to solve the model parameter uncertainness, which is particularly suitable for solving the unconstrained optimization problem. In summary, the main contributions of this article are as follows.

1) Analysis of the prediction error due to the model parameter uncertainties is proposed. The results indicate that the prediction errors are mainly influenced by variations in filter parameters, the grid voltage, and the inverter voltage. The prediction error is more serious when the actual value is smaller than the modeled one.
2) To achieve fast and high accuracy parameter estimation, a variable learning rate naming RMSprop-GDO is proposed. Thus, the model parameters used in FCS-MPC are estimated and updated periodically. In this way, the parameter mismatches can be solved and power quality of the grid current is enhanced.

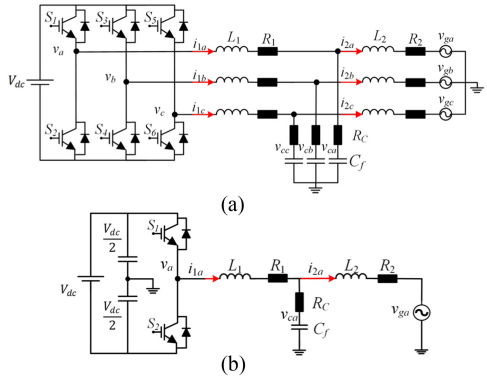


Fig. 1. Topology of a three-phase two-level *LCL*-GCCs. (a) Three-phase model. (b) Per-phase model of the three-phase converter.

This article is arranged as follows. Section II describes the prediction model and FCS-MPC control of the three-phase *LCL*-GCCs. Section III analyzes the prediction errors of the state variables due to the mismatched model parameters. Section IV, first, presents the parameter identification method with the RMSprop-GDO. Then, the online filter parameter identification with the variable iteration step is described. Furtherly, the block diagram and implementation flowchart of the proposed method are elaborated. Finally, stability analysis of the *LCL*-GCCs with RMSprop-GDO based FCS-MPC are performed. To confirm the effectiveness of the proposed method, Section V presents the experimental verification results. Finally, Section VI concludes this article.

II. System Model and FCS-MPC Control

In this section, the topology and modeling of the *LCL*-GCCs are described at first. Then, the FCS-MPC control method is discussed.

A. Topology of the Three-Phase LCL-GCCs

Fig. 1(a) depicts the system analyzed in this article. It consists of a three-phase voltage-source-converter (VSC) connected to the grid through an *LCL* filter, which is equivalent to three parallel connected single-phase system [as shown in Fig. 1(b)]. The control algorithm is calculated in a digital signal processor (DSP) in $\alpha\beta$ stationary-frame since all three-phase quantities in the natural reference frame were changed to this basis. In Fig. 1, $V_{\rm dc}$ is the dc-link voltage; v_a, v_b, and v_c are the converter-side voltages; v_{ca}, v_{cb}, and v_{cc} are the filter capacitor voltages; v_{ga}, v_{gb}, and v_{gc} are the grid voltages; i_{1a}, i_{1b}, and i_{1c} are the converter-side currents; i_{ga}, i_{gb}, and i_{gc} are the grid currents; L_1 and L_2 are the converter and grid side filter inductances; R_1

Authorized licensed use limited to: Universidad Andres Bello. Downloaded on June 25,2024 at 19:34:06 UTC from IEEE Xplore. Restrictions apply.

is the parasitic resistance of L_1; R_2 is the parasitic resistance of L_2; C_f is the filter capacitance; and R_c is the passive damping resistor.

Assuming the switching components of the system are ideal, at any given instance, each phase of the three-phase system may only contain one of two possible switching states in the finite control set as

$$\boldsymbol{S_{abc}} = [s_a, s_b, s_c]^T \tag{1}$$

where $s_a, s_b, s_c \in (-11)$; "$s = 1$" means that the upper bridge power transistor is in the ON state and the lower bridge power transistors are in the OFF state. "$s = -1$" means that the lower bridge switches are ON and the upper bridge switches are OFF. The relationship between switching state $\boldsymbol{S_{abc}}$ and inverter voltage $\boldsymbol{v}_{inv}(k)$ is shown as

$$\boldsymbol{v}_{inv} = \frac{V_{dc}}{2}\boldsymbol{S_{abc}}. \tag{2}$$

B. Discrete Model

To get the discrete-time state-space model of the GCCs, the state variable of the system $\boldsymbol{x}(t)$ in (3) is defined as $\boldsymbol{x}(t) = [\boldsymbol{i}_1(t), \boldsymbol{i}_2(t), \boldsymbol{v_c}(t)]^T$, where $\boldsymbol{i_1}$, $\boldsymbol{i}_2$, and $\boldsymbol{v_c}$ are the vectors for three-phase converter-side current, grid-side current, capacitor voltage, respectively. $\boldsymbol{v_{inv}}$ and $\boldsymbol{v_g}$ are converter voltage, and grid voltage, respectively, which are defined as

$$\begin{cases} \boldsymbol{i}_1(t) = [i_{1a}, i_{1b}, i_{1c}]^T \\ \boldsymbol{i}_2(t) = [i_{2a}, i_{2b}, i_{2c}]^T \\ \boldsymbol{v_c}(t) = [v_{ca}, v_{cb}, v_{cc}]^T \\ \boldsymbol{v_g}(t) = [v_{ga}, v_{gb}, v_{gc}]^T \\ \boldsymbol{v_{inv}}(t) = [v_a, v_b, v_c]^T \end{cases}. \tag{3}$$

According to Kirchhoff's law, the circuit equation for $\boldsymbol{L}_1, \boldsymbol{L}_2$, $\boldsymbol{C_f}$, $\boldsymbol{R}_1$, $\boldsymbol{R}_2$, and $\boldsymbol{R_C}$ can be derived as

$$\begin{cases} \boldsymbol{L}_1\frac{d\boldsymbol{i}_1}{dt} + \boldsymbol{R_C C_f}\frac{d\boldsymbol{v_c}}{dt} = -\boldsymbol{i}_1\boldsymbol{R}_1 - \boldsymbol{v_c} + \boldsymbol{v_{inv}} \\ \boldsymbol{L}_2\frac{d\boldsymbol{i}_2}{dt} - \boldsymbol{R_C C_f}\frac{d\boldsymbol{v_c}}{dt} = -\boldsymbol{i}_2\boldsymbol{R}_2 + \boldsymbol{v_c} - \boldsymbol{v_g} \\ \boldsymbol{C_f}\frac{d\boldsymbol{v_c}}{dt} = \boldsymbol{i}_1 - \boldsymbol{i}_2 \end{cases} \tag{4}$$

where $\boldsymbol{L}_1 = L_1\boldsymbol{I}_{3\times3}$, $\boldsymbol{L}_2 = L_2\boldsymbol{I}_{3\times3}$, $\boldsymbol{C_f} = C_f\boldsymbol{I}_{3\times3}$, $\boldsymbol{R}_1 = R_1\boldsymbol{I}_{3\times3}$, $\boldsymbol{R}_2 = R_2\boldsymbol{I}_{3\times3}$, $\boldsymbol{R_C} = R_C\boldsymbol{I}_{3\times3}$, and $\boldsymbol{I}_{i\times i}$ is the ith order unit matrix.

The continuous-time state-space model in (4) can be simplified as

$$\begin{cases} \alpha\frac{d\boldsymbol{x}(t)}{dt} = \beta x(t) + \gamma u(t) + \delta\boldsymbol{v}_g(t) \\ y(t) = \lambda x(t) \end{cases} \tag{5}$$

where $\boldsymbol{u} = [T_a\ T_b\ T_c]^{\boldsymbol{T}}$, $\boldsymbol{\alpha}$, $\boldsymbol{\beta}$, $\boldsymbol{\gamma}$, and $\boldsymbol{\delta}$ are all constant matrixes. T_a, T_b, and T_c are the duty-ratio of the upper three-legs, respectively. Assume $\boldsymbol{O}_{i\times j}$ is the empty matrix with i-row and j-column. Therefore, $\boldsymbol{\alpha}$, $\boldsymbol{\beta}$, $\boldsymbol{\gamma}$, and $\boldsymbol{\delta}$ can be expressed as

$$\boldsymbol{\alpha} = \begin{pmatrix} \boldsymbol{L}_1 & \boldsymbol{O}_{3\times3} & \boldsymbol{R_C C_f} \\ \boldsymbol{O}_{3\times3} & \boldsymbol{L}_2 & -\boldsymbol{R_C C_f} \\ \boldsymbol{O}_{3\times3} & \boldsymbol{O}_{3\times3} & \boldsymbol{C_f} \end{pmatrix}$$

$$\boldsymbol{\beta} = \begin{pmatrix} -\boldsymbol{R}_1 & \boldsymbol{O}_{3\times3} & -\boldsymbol{I}_{3\times3} \\ \boldsymbol{O}_{3\times3} & -\boldsymbol{R}_2 & \boldsymbol{I}_{3\times3} \\ \boldsymbol{I}_{3\times3} & -\boldsymbol{I}_{3\times3} & \boldsymbol{O}_{3\times3} \end{pmatrix}$$

$$\boldsymbol{\gamma} = \left(\frac{V_{\rm dc}}{2}\boldsymbol{I}_{3\times3}\boldsymbol{O}_{3\times6}\right)^{\boldsymbol{T}}$$

$$\boldsymbol{\delta} = (\boldsymbol{O}_{3\times3} - \boldsymbol{I}_{3\times3}\boldsymbol{O}_{3\times3})^{\boldsymbol{T}}.$$

Equation (5) can be changed into the standard form of a state-space equation given as

$$\begin{cases} \frac{d\boldsymbol{x}(t)}{dt} = Fx(t) + Gu(t) + P\boldsymbol{v}_g(t) \\ y(t) = \lambda x(t) \end{cases} \tag{6}$$

where $\boldsymbol{F}$, $\boldsymbol{G}$, and $\boldsymbol{P}$ are the parameter matrixes of the circuit, $\boldsymbol{F} = \boldsymbol{\alpha}^{-1} \times \boldsymbol{\beta}$, $\boldsymbol{G} = \boldsymbol{\alpha}^{-1}\boldsymbol{\gamma}$, $\boldsymbol{P} = \boldsymbol{\alpha}^{-1}\boldsymbol{\delta}$. $\boldsymbol{y}(t)$ is the weight redistribution of the state variable $\boldsymbol{x}(t)$, $\boldsymbol{\lambda} = [\lambda_1\boldsymbol{I}_{1\times3}\ \lambda_2\boldsymbol{I}_{1\times3}]$ is the weight factor vector for the inverter-side current $\boldsymbol{i}_1$and the grid current $\boldsymbol{i}_2$. Then, $\boldsymbol{y} = [\lambda_1\boldsymbol{i}_1\ \lambda_2\boldsymbol{i}_2]^{\boldsymbol{T}}$.

By using Du Hamel integral formula [40] to discretize (6), the discretized-time state-space equation can be obtained as

$$\begin{cases} x(k+1) = Ax(k) + Bu(k) + T\boldsymbol{v}_g(k) \\ y(k) = \lambda x(k) \end{cases} \tag{7}$$

where $\boldsymbol{A} = e^{\boldsymbol{F}T_s}$, $\boldsymbol{B} = -\boldsymbol{F}^{-1}(\boldsymbol{I}_{9\times9} - \boldsymbol{A})\boldsymbol{G}$, $\boldsymbol{T} = -\boldsymbol{F}^{-1}(\boldsymbol{I}_{9\times9} - \boldsymbol{A})\boldsymbol{P}$. However, (7) cannot accurately describe the system for two reasons: first, there are sampling errors during the discretization; second, the filter parameters L_1, L_2, and C in $\boldsymbol{A}, \boldsymbol{B},$ and $\boldsymbol{T}$ may deviate from their nominal values, which may lead to parameter mismatch and degrade the performance of FCS-MPC control of the GCCs.

To simplify the calculation and avoid the coupling between active and reactive current components, the three-phase state-space equation in (7) are transformed into $\alpha\beta$-coordinates, thus, the state-space (7) under $\alpha\beta$-frame is written as

$$\begin{cases} \boldsymbol{x}_{\alpha\beta}\ (k+1) = \boldsymbol{A}_{\alpha\beta}\,\boldsymbol{x}_{\alpha\beta}(k) + \boldsymbol{B}_{\alpha\beta}u(k) + \boldsymbol{T}_{\alpha\beta}\boldsymbol{v}_{g\alpha\beta}(k) \\ \boldsymbol{y}_{\alpha\beta}\ (k) = \boldsymbol{\lambda}_{\alpha\beta}\,\boldsymbol{x}_{\alpha\beta}(k) \end{cases} \tag{8}$$

where $\boldsymbol{x}_{\alpha\beta}$, $\boldsymbol{A}_{\alpha\beta}$, $\boldsymbol{B}_{\alpha\beta}$, $\boldsymbol{T}_{\alpha\beta}$, $\boldsymbol{v}_{g\alpha\beta}$, $\boldsymbol{y}_{\alpha\beta}$, and $\boldsymbol{\lambda}_{\alpha\beta}$ are the matrix of $\boldsymbol{x}$, $\boldsymbol{A}$, $\boldsymbol{B}$, $\boldsymbol{T}$, $\boldsymbol{v}$, $\boldsymbol{y}$, and $\boldsymbol{\lambda}$ in (7) under $\alpha\beta$-coordinates. The discrete-model of (8) is implemented in FCS-MPC controller.

C. FCS-MPC Control of the LCL-GCCs

The FCS-MPC uses the discrete nature of the power electronic converters to reduce the computational burden of the MPC algorithm [41]. The converter has a finite number of switching states, so the optimization problem is solved only for this set of operation points. The discrete model of the three-phase *LCL*-GCCs, presented in (8), is used to predict the output variables for the next sampling instant $\boldsymbol{y}_{\alpha\beta}(k+1)$. In this article, the *LCL*-GCCs is constituted by a three-phase two-level VSC with an *LCL*-filter, which is commonly used in distributed generation system. Nevertheless, one of the major advantages of the FCS-MPC is its capability to easily extend the concepts presented here for use in three-phase or multiphase inverters.

The goal of GCCs control is to ensure that the power converter provides high power quality of the grid current integration with the grid. Meanwhile, the power consumption generated due to the switching frequency of the power transistors should be kept to the minimum. To avoid over current protection of the relays on

Authorized licensed use limited to: Universidad Andres Bello. Downloaded on June 25,2024 at 19:34:06 UTC from IEEE Xplore. Restrictions apply.

converter-side of the GCCs and improve the transient response of the grid current, both converter-side and grid-side current are controlled, the converter-side current reference is calculated by the grid current reference and capacitor voltage [42]. In steady-state, the grid-side current should have only small tracking errors and minor harmonic distortion. The dynamic response of the grid current such as overshoot, fast time-response, and switching losses should also be guaranteed. Considering the multiobject optimization issues, the cost function (CF) $\boldsymbol{g}$ is designed as

$$\begin{aligned}\boldsymbol{g} = &\boldsymbol{\lambda}_{1\alpha\beta}\|\boldsymbol{i}_{1\mathrm{ref}\alpha\beta}(k+1) - \boldsymbol{i}_{1\alpha\beta}(k+1)\|^2 \\ &+ \boldsymbol{\lambda}_{2\alpha\beta}\|\boldsymbol{i}_{2\mathrm{ref}\alpha\beta}(k+1) - \boldsymbol{i}_{2\alpha\beta}(k+1)\|^2 \\ &+ \lambda_u\|\boldsymbol{S}_{abc}(k) - \boldsymbol{S}_{abc}(k-1)\|^2 \end{aligned} \tag{9}$$

where $\|\cdot\|$ stands for the Euclidean 2-norms of the vector, λ_u is the weight factor for minimizing the switching loss, $\boldsymbol{i}_{1\mathrm{ref}\alpha\beta}$, and $\boldsymbol{i}_{2\mathrm{ref}\alpha\beta}$ are the reference vector. $\boldsymbol{i}_{1\alpha\beta}$ and $\boldsymbol{i}_{2\alpha\beta}$ are the predicted component under $\alpha\beta$-coordinates, respectively. $\boldsymbol{\lambda}_{\alpha\beta} = [\,\lambda_{1\alpha\beta}\ \lambda_{2\alpha\beta}\,]$ is the weight factor vector for converter-side and grid-side current. The converter switch state $\boldsymbol{S}_{abc}$ corresponding to the minimum objective function is defined as the optimal value, and the switching vector corresponding to the minimal $\boldsymbol{g}$ is the optimal switching vector, which directly acts on the inverter switching devices as the control signal.

In practice, due to two reasons that converter-side current needs are considered. First, it is needed to consider the over-current protection of the system when the overload occurs. Without limiting the converter-side current, the GCCs may break down whenever an overcurrent fault occurs. This is because the converter-side current has faster response time than that of the grid current in case of an overcurrent fault. The overcurrent may endanger the reliability of the system. Seriously, the *LCL*-GCCs may break down. Second, theoretically speaking, the dynamic response of the grid current can be improved by the converter-side current. Thereby, both converter-side and grid-side current control are considered in CF. Thus, $\lambda_{1\alpha\beta} = \lambda_{2\alpha\beta} = 1$ in (9) are applied to the cost function [43], [44].λ_u is the only weigh factor tuned in experiment to achieve a compromise between the power quality of the grid current and the switching losses.

III. Prediction Error Analysis Due to Filter Parameter Variations

A. Prediction Error Equation Due to Model Parameter Mismatch

Model parameter mismatch will affect the predicted value and lead to prediction error. Previous research has shown that resistance mismatch of the filter will influence the steady-state error in the grid current prediction [27], [45]. However, the inductance and capacitance mismatches will impact both the steady-state and transient response of the grid current [46]. Therefore, this article focuses on variations in the filter inductance and the capacitance.

To analyze the variations of filter parameters on the impact of the prediction errors in abc-coordinates and separate the variable parameters from the constants, defining the diagonal matrix $\boldsymbol{L}$ as

$$\boldsymbol{L} = \begin{bmatrix} T_s/\boldsymbol{L}_1 & 0 & 0 \\ 0 & T_s/\boldsymbol{L}_2 & 0 \\ 0 & 0 & T_s/\boldsymbol{C_f} \end{bmatrix}. \tag{10}$$

$\boldsymbol{L}$ should be a diagonal matrix so that the discrete-time state-space equation of (7) and (11) are equal. In addition, the variable parameter matrix $\boldsymbol{L}_1$, $\boldsymbol{L}_2$, and $\boldsymbol{C_f}$ are separated from the constant matrix $\boldsymbol{F'}$. Then, by forward Euler method, the predictive (11) can be derived as

$$\boldsymbol{x}_{\mathrm{est}}(k+1) = (\boldsymbol{I} + \boldsymbol{L}\boldsymbol{F'})\,\boldsymbol{x}(k) + \boldsymbol{L}\boldsymbol{G'}\boldsymbol{v_{inv}}(k) + \boldsymbol{L}\boldsymbol{P'}\boldsymbol{v}_g(k) \tag{11}$$

where $\boldsymbol{x}_{\mathrm{est}}(k+1)$ is the state variable at instant $k+1$, $\boldsymbol{F'} = \boldsymbol{L}^{-1}\,\boldsymbol{F}T_s$, $\boldsymbol{G'} = \boldsymbol{L}^{-1}\,\boldsymbol{G}T_s$, and $\boldsymbol{P'} = \boldsymbol{L}^{-1}\,\boldsymbol{P}T_s$, which are given as

$$\boldsymbol{F'} = \begin{bmatrix} -(\boldsymbol{R}_c + \boldsymbol{R}_1) & \boldsymbol{R}_c & -\boldsymbol{I}_{3\times3} \\ \boldsymbol{R}_c & -(\boldsymbol{R}_c + \boldsymbol{R}_2) & \boldsymbol{I}_{3\times3} \\ \boldsymbol{I}_{3\times3} & -\boldsymbol{I}_{3\times3} & \boldsymbol{O}_{3\times3} \end{bmatrix}$$

$$\boldsymbol{G'} = \begin{bmatrix}\boldsymbol{I}_{3\times3}\ \boldsymbol{O}_{3\times3}\ \boldsymbol{O}_{3\times3}\end{bmatrix}^T,$$

$$\boldsymbol{P'} = \begin{bmatrix}\boldsymbol{O}_{3\times3}\ -\boldsymbol{I}_{3\times3}\ \boldsymbol{O}_{3\times3}\end{bmatrix}^T.$$

For the parameter uncertainties in the *LCL*-filter, the variations in the resistances $\boldsymbol{R}_c$, $\boldsymbol{R}_1$, and $\boldsymbol{R}_2$ have little influence in prediction error compared to the inductance and capacitance. Thus, only the variations of the inductances $\Delta\boldsymbol{L}_1$ and $\Delta\boldsymbol{L}_2$ and the capacitance $\Delta\boldsymbol{C_f}$ are considered. Assuming the changes in the diagonal parameter matrix $\boldsymbol{L'}$ are given as

$$\boldsymbol{L'} = \begin{bmatrix} \frac{T_s}{(\boldsymbol{L}_1+\Delta\boldsymbol{L}_1)} & \boldsymbol{O}_{3\times3} & \boldsymbol{O}_{3\times3} \\ \boldsymbol{O}_{3\times3} & \frac{T_s}{(\boldsymbol{L}_2+\Delta\boldsymbol{L}_2)} & \boldsymbol{O}_{3\times3} \\ \boldsymbol{O}_{3\times3} & \boldsymbol{O}_{3\times3} & \frac{T_s}{(\boldsymbol{C}_f+\Delta\boldsymbol{C}_f)} \end{bmatrix}. \tag{12}$$

Then, the prediction equation under parameter mismatch can be written as

$$\begin{aligned}\boldsymbol{x'}_{\mathrm{est}}(k+1) = &(\boldsymbol{I} + \boldsymbol{L'}\boldsymbol{F'})\,\boldsymbol{x}(k) + \boldsymbol{L'}\boldsymbol{G'}\boldsymbol{v}_{inv}(k) \\ &+ \boldsymbol{L'}\boldsymbol{P'}\boldsymbol{v}_g(k). \end{aligned} \tag{13}$$

where $\boldsymbol{x'}_{\mathrm{est}}(k+1)$ is the state variables with mismatched parameters at time instant $k+1$. Thus, the prediction error $\boldsymbol{\Delta x}$ at instant $k+1$ can be written as

$$\begin{aligned}\boldsymbol{\Delta x}(k+1) &= \boldsymbol{x'}_{\mathrm{est}}(k+1) - \boldsymbol{x}_{\mathrm{est}}(k+1) \\ &= (\boldsymbol{L'} - \boldsymbol{L})\,(\boldsymbol{F'}\boldsymbol{x}(k) + \boldsymbol{G'}\boldsymbol{v}_{inv}(k) + \boldsymbol{P'}\boldsymbol{v}_g(k)). \end{aligned} \tag{14}$$

Equation (14) indicates that, for the given grid and converter side voltages, the prediction errors of the state variable are influenced by the deviations in the filter parameter.

B. Effects of Model Uncertainty

From Fig. 1, according to Kirchhoff's law, to simplify the analysis, taking phase-a of the three-phase system as an example, the variables and filter parameters in this section and Section IV are defined and used for phase-a. Compared with the impedance

Authorized licensed use limited to: Universidad Andres Bello. Downloaded on June 25,2024 at 19:34:06 UTC from IEEE Xplore. Restrictions apply.

of L_1 and L_2, the resistance of R_1 and R_2 are very small, which can be ignored. The gird current $i_2(s)$ can be derived as

$$i_2(s) = \frac{sC_fR_c+1}{s^3L_1L_2C_f+s^2(L_1+L_2)C_fR_c+s(L_1+L_2)}v_{inv} - \frac{1}{s^3L_1L_2C_f+s^2(L_1+L_2)C_fR_c+s(L_1+L_2)}v_g. \tag{15}$$

Assuming L_{10}, L_{20}, and C_{f0} are the nominal values of the *LCL*-filter. $\Delta L_1, \Delta L_2$, and ΔC_f are the parameter deviations of the *LCL*-filter. Thus, $L_1 = L_{10} + \Delta L_1$, $L_{20} = L_{20} + \Delta L_2$, $C_f = C_{f0} + \Delta C_f$. The deviation of $i_2(s)$ can be derived as

$$\Delta i_2(s) = i_2(s) - i_{20}(s) = \left(\frac{1}{D_1(s)} - \frac{1}{D_0(s)}\right) \times \left((sR_c+1)v_{inv} - v_g\right)\frac{sR_c\Delta C_f}{D_1(s)} \tag{16}$$

where $D_0(s)$, $D_1(s)$, and $\Delta D(s)$ are the denominators of (15) with the nominal value, with the mismatched value, and the difference of $D_0(s)$ and $D_1(s)$, respectively, which is given as

$$\begin{aligned} D_0(s) &= s^3L_{10}L_{20}C_{f0} + s^2(L_{10}+L_{20})C_{f0}R_c + s(L_{10}+L_{20}) \\ D_1(s) &= s^3L_1L_2C_f + s^2(L_1+L_2)C_fR_c + s(L_1+L_2) \\ \Delta D(s) &= D_1(s) - D_0(s) \approx s^3(L_{10}C_{f0}\Delta L_2 + L_{20}C_{f0}\Delta L_1 + L_{10}L_{20}\Delta C_f) \\ &\quad + s^2((\Delta L_1+\Delta L_2)C_{f0} + (L_{10}+L_{20})\Delta C_f)R_c \\ &\quad + s(\Delta L_1+\Delta L_2). \end{aligned}$$

Thus, the ratio between $\Delta i_2(s)$ and $i_{20}(s)$ can be derived as

$$\frac{\Delta i_2(s)}{i_{20}(s)} = \frac{\Delta D(s)(v_g-(sR_cC_{f0}+1)v_{inv})+sR_c\Delta C_{f0}D_0(s)}{(D_0(s)+\Delta D(s))((sR_cC_{f0}+1)v_{inv}-v_g)} = \frac{\frac{sR_c\Delta C_{f0}}{(sR_cC_{f0}+1)v_{inv}-v_g} - \frac{\Delta D(s)}{D_0(s)}}{1+\frac{\Delta D(s)}{D_0(s)}} \tag{17}$$

where $\Delta D(s)/D_0(s)$ can be derived as unnumbered equation shown at the bottom of this page.

Hence, the prediction error of $i_2(s)$ can be given by (17). With the filter parameters in given Table I, Fig. 2 shows the magnitude of the grid current prediction errors $\Delta i_2(s)/i_{20}(s)$ with uncertainty parameters. The mismatches of L_1, L_2, and C_f are analyzed with the uncertainties K varying between -20% and 20% of their nominal value. At 50 Hz, $\Delta i_2(s)/i_{20}(s)$ is 0.249 with negative deviation coefficient $k = -0.2$ compared to 0.166 with positive deviation coefficient $k = 0.2$, indicating that the prediction error is more serious when the actual filter parameters are smaller than the modeled one. Meanwhile, the prediction errors are also influenced by the inverter-side and grid voltage. If the *LCL*-filter parameters can be observed with high accuracy, the modeling errors in MPC can be reduced. Thus, the tracking errors of the grid current with FCS-MPC controller can be minimized.

TABLE I
EXPERIMENTAL PARAMETERS

Symbol	Parameter	Value
V_{dc}	DC voltage	700 V
v_g	Grid voltage	$220\sqrt{2}$ V
L_1	Converter side inductance	4 mH
L_2	Grid side inductance	2 mH
R_1	Parasitic resistance of L_1	1 $m\Omega$
R_2	Parasitic resistance of L_2	1 $m\Omega$
C_f	Capacitance	10 μF
R_c	Passive damping resistor	25 Ω
T_s	Sample time	20 μs

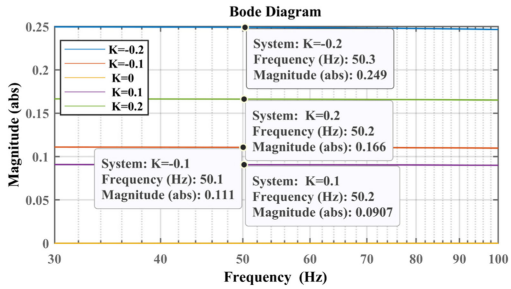


Fig. 2. Prediction errors of the grid current influenced by filter parameter mismatches.

IV. PARAMETER IDENTIFICATION REALIZATION AND STABILITY ANALYSIS

A. Realization of GDO

Assuming $\boldsymbol{x}_{\text{est}}(k)$ is the estimated value at instant $k-1$, and because of the parameter mismatch, there must be some errors between $\boldsymbol{x}_{\text{est}}(k)$ and $\boldsymbol{x}(k)$. The error vector $\boldsymbol{E}(k)$ between the sampled and estimated values at instant k is defined as

$$\boldsymbol{E}(k) = \boldsymbol{x}(k) - \boldsymbol{x}_{\text{est}}(k). \tag{18}$$

Ignoring the error caused by discretization, the error vector $\boldsymbol{E}(k)$ is generated due to the variation of parameter matrix $\Delta\boldsymbol{L}$. By calculating $\Delta\boldsymbol{L}$ at each sampling time via adaptive algorithm, the parameter matrix can approach the actual value. The block diagram of the adaptive parameter identification based on GDO is shown in Fig. 3.

The adaptive algorithm in Fig. 3 adopts GDO, meaning that it descends in the opposite direction for the gradient of the objective function and finds the corresponding parameter matrix $\boldsymbol{L}$ when searching the minimum value of the objective function.

The objective function is defined as

$$\boldsymbol{J_d} = 1/2\boldsymbol{E}^T(k)\boldsymbol{E}(k). \tag{19}$$

$$\frac{\Delta D(s)}{D_0(s)} = \frac{s^2\left(\frac{\Delta L_2}{L_{20}}+\frac{\Delta L_1}{L_{10}}+\frac{\Delta C_f}{C_{f0}}\right)+s\left(\frac{(\Delta L_1+\Delta L_2)}{L_{10}+L_{20}}+\frac{(L_{10}+L_{20})}{L_{10}L_{20}}\cdot\frac{\Delta C_f}{C_{f0}}\right)R_c+\frac{(\Delta L_1+\Delta L_2)}{L_{10}L_{20}}\cdot\frac{1}{C_{f0}}}{s^2+s\frac{(L_{10}+L_{20})}{L_{10}L_{20}}R_c+\frac{(L_{10}+L_{20})}{L_{10}L_{20}}\cdot\frac{1}{C_{f0}}}$$

Authorized licensed use limited to: Universidad Andres Bello. Downloaded on June 25,2024 at 19:34:06 UTC from IEEE Xplore. Restrictions apply.

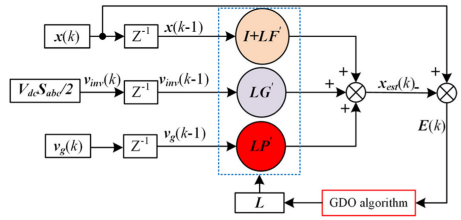


Fig. 3. Parameter identification with GDO method.

The minimum J_d can be found by calculating the gradient of the objective function $\boldsymbol{J_d}$ along with the parameter matrix $\boldsymbol{L}$ direction, i.e., finding the minimum $\boldsymbol{E}(k)$. If $\boldsymbol{E}(k)$ is minimal, the change in the parameter matrix $\boldsymbol{L}$ is close to 0, and the updated parameters are consistent with the real values.

The gradient matrix of $\boldsymbol{J_d}$ along with the variable matrix $\boldsymbol{L}$ is defined as follows:

$$\frac{\partial \boldsymbol{J_d}}{\partial \boldsymbol{L}} = \begin{bmatrix} \frac{\partial J_d}{\partial L_{11}} & \frac{\partial J_d}{\partial L_{12}} & \frac{\partial J_d}{\partial L_{13}} \\ \frac{\partial J_d}{\partial L_{21}} & \frac{\partial J_d}{\partial L_{22}} & \frac{\partial J_d}{\partial L_{23}} \\ \frac{\partial J_d}{\partial L_{31}} & \frac{\partial J_d}{\partial L_{32}} & \frac{\partial J_d}{\partial L_{33}} \end{bmatrix} = \begin{bmatrix} \frac{\partial J_d}{\partial L_{11}} & 0 & 0 \\ 0 & \frac{\partial J_d}{\partial L_{22}} & 0 \\ 0 & 0 & \frac{\partial J_d}{\partial L_{33}} \end{bmatrix} \tag{20}$$

where $\boldsymbol{J}_d = 1/2\boldsymbol{E}^T(k)\boldsymbol{E}(k) = 1/2(e_{i1}^2+e_{i2}^2+e_{vc}^2)$, $e_{i1} = \Delta i_1$, $e_{i2} = \Delta i_2$, and $e_{vc} = \Delta v_c$, which are the errors of the filter parameters. Considering that all other elements except for the diagonal elements of the gradient matrix $\partial \boldsymbol{J}_d/\partial \boldsymbol{L}$ are zero, then, the gradient of $\boldsymbol{J}_d$ along with $\boldsymbol{L}$ are given as

$$\frac{\partial J_d}{\partial L_{11}} = \frac{1}{2}\frac{\partial e_{i1}^2}{\partial L_{11}} = e_{i1}\frac{\partial e_{i1}}{\partial L_{11}} \quad \frac{\partial J_d}{\partial L_{22}} = \frac{1}{2}\frac{\partial e_{i2}^2}{\partial L_{22}} = e_{i2}\frac{\partial e_{i2}}{\partial L_{22}}$$
$$\frac{\partial J_d}{\partial L_{33}} = \frac{1}{2}\frac{\partial e_{vc}^2}{\partial L_{33}} = e_{vc}\frac{\partial e_{vc}}{\partial L_{33}}.$$

Therefore, (20) can be rearranged as

$$\frac{\partial \boldsymbol{J}_d}{\partial \boldsymbol{L}} = \begin{bmatrix} e_{i1} \\ e_{i2} \\ e_{vc} \end{bmatrix} \begin{bmatrix} \frac{\partial e_{i1}}{\partial L_{11}} & \frac{\partial e_{i2}}{\partial L_{22}} & \frac{\partial e_{vc}}{\partial L_{33}} \end{bmatrix} = \boldsymbol{E}(k)\frac{\partial \boldsymbol{E}(k)^T}{\partial \boldsymbol{L}}$$

where

$$\frac{\partial \boldsymbol{E}(k)}{\partial \boldsymbol{L}} = -\left[\boldsymbol{A'x}(k-1) + \boldsymbol{B'^{v_{inv}}}(k-1) + \boldsymbol{T'^{v_g}}(k-1)\right].$$

Thus, the gradient matrix of the objective function $\boldsymbol{J}_d$ along $\boldsymbol{L}$ can be expressed as

$$\begin{aligned} \boldsymbol{G_L}(k) &= \partial \boldsymbol{J}_d/\partial \boldsymbol{L} = -\boldsymbol{E}(k)\frac{\partial \boldsymbol{E}(k)}{\partial \boldsymbol{L}} \\ &= -\boldsymbol{E}(k)\left[\boldsymbol{A'x}(k-1) + \boldsymbol{B'v}(k-1)\right. \\ &\quad \left. + \boldsymbol{T'v}_g(k-1)\right]^T. \end{aligned} \tag{21}$$

The diagonal element of the gradient matrix $\boldsymbol{G}_L$ is the variation in the parameter matrix $\boldsymbol{L}$, and the values of the OFF-diagonal elements are meaningless. When the gradient descent is carried out and $\Delta \boldsymbol{L}$ is selected as the iterative matrix, the rest elements of $\Delta \boldsymbol{L}$ are 0. $\Delta \boldsymbol{L}$ can be written as

$$\Delta \boldsymbol{L} = \begin{bmatrix} G_{L11} & 0 & 0 \\ 0 & G_{L22} & 0 \\ 0 & 0 & G_{L33} \end{bmatrix}. \tag{22}$$

The parameter matrix $\boldsymbol{L}$ at instant k is

$$\boldsymbol{L}(k) = \boldsymbol{L}(k-1) - \Lambda \Delta \boldsymbol{L}(k) \tag{23}$$

where Λ is the iteration step length matrix of $\boldsymbol{L}$, defined as

$$\Lambda = \begin{bmatrix} \eta_1 & 0 & 0 \\ 0 & \eta_2 & 0 \\ 0 & 0 & \eta_3 \end{bmatrix}$$

where η_1, η_2, and η_3 are the learning rates of the three elements corresponding to the parameter matrix $\boldsymbol{L}$, respectively.

After setting the learning rate, the parameter matrix $\boldsymbol{L}$ will gradually approach its actual value. Thus, the observed results of the three parameters (L_1, L_2, and C_f) at instant k can be obtained as

$$\begin{cases} L_{1\text{new}}(k) = T_s/L_{11}(k) \\ L_{2\text{new}}(k) = T_s/L_{22}(k) \\ C_{f\text{new}}(k) = T_s/L_{33}(k) \end{cases}. \tag{24}$$

It is needed to note that the proposed GDO method is also applicable under weak grid conditions, this is because when the grid impedance changes, the grid voltage and current at the point of common coupling will vary accordingly, thereby parameter identification results of the proposed method will not be influenced.

B. RMSprop-GDO for Learning Rate Improvement

From the analysis of the iteration step size in Section A, learning rate is an important parameter in the gradient descent algorithm. When it is very small, the filter parameter identification time will last long time, but when it is too large, it leads to the training oscillation and may diverge. An ideal gradient descent algorithm should satisfy two requirements: fast convergence speed and global convergence. In this article, the RMSprop-based variable learning rate is used, which mainly solves the rapid attenuation problem of the learning rate. Similar to the momentum idea, the introduction of a hyperparameter in the accumulation of gradient square term attenuation is given as

$$\begin{cases} s \leftarrow \gamma \cdot s + (1-\gamma) \cdot \nabla \boldsymbol{J}(\boldsymbol{L}) \odot \nabla \boldsymbol{J}(\boldsymbol{L}) \\ \boldsymbol{L} \leftarrow \boldsymbol{L} - \frac{\Lambda}{\sqrt{s+\varepsilon}} \odot \nabla \boldsymbol{J}(\boldsymbol{L}) \end{cases} \tag{25}$$

where s is the exponential weighted moving average of the gradient square, γ is generally chosen as 0.9. In addition, s is more stable at this moment, which reduces the explosion situation, so it helps to avoid the fast decline problem in the learning rate. ε is very small as to prevent a zero in the denominator of (25), here ε is set to 0.001.

C. FCS-MPC Control of the LCL-GCCs With RMSprop-GDO Method

The block diagram and implementation of the FCS-MPC controlled *LCL*-GCCs with RMSprop-GDO method is shown in Fig. 4, which includes the blocks named as: cost function calculation and optimal control sequence selection, GDO-based parameter identification method, learning rate improvement

Authorized licensed use limited to: Universidad Andres Bello. Downloaded on June 25,2024 at 19:34:06 UTC from IEEE Xplore. Restrictions apply.

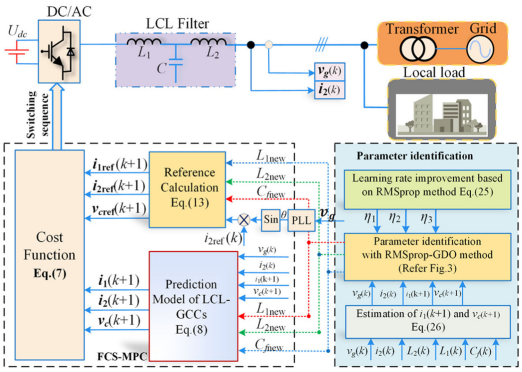


Fig. 4. Block diagram of the FCS-MPC controlled *LCL*-GCCs with the proposed RMSprop-GDO method.

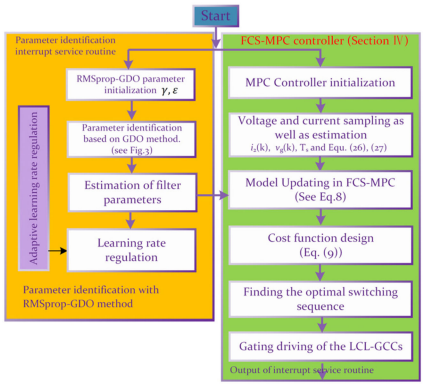


Fig. 5. Implementation flow chart of the proposed RMSprop-GDO method.

based on RMSprop method, reference current calculation, and FCS-MPC controller.

To reduce the voltage and current sensors in Fig. 3, the sampling for v_c and i_1 can be avoided, which can be indirectly concluded by other variables. The expressions for v_c and i_1 can be concluded by v_g, i_2, and T_s, which is given by (26) shown at the bottom of this page. With the help of Fig. 3, the filter parameters (L_{1new}, $L_{2\text{new}}$, and $C_{f\text{new}}$) can be estimated by RMSprop-GDO method. Thus, the filter parameters in FCS-MPC control and (26) can be periodically updated by the estimated results given by

$$\begin{aligned} &L_1(k+1) = L_{1\text{new}}(k), L_2(k+1) = L_{2\text{new}}(k) \\ &C_f(k+1) = C_{f\text{new}}(k). \end{aligned} \tag{27}$$

Fig. 5 shows the implementation flowchart of Fig. 4. There are mainly two interrupt service routine, one is used for the normal FCS-MPC control, the other is applied for the parameter identification and updating.

For the normal FCS-MPC interrupt service routine, first, the parameters of the FCS-MPC controller are initialized. Second, the three-phase voltage and current sampling signals, e.g., $\boldsymbol{i}_2$ and $\boldsymbol{v}_g$ are transmitted to the microprocessor. To avoid the coupling between active and reactive current components in dq-coordinate, alpha-beta transformation is applied. Thereby, the sampled results under the $\alpha\beta$-frame are obtained and served as the inputs of the prediction model in (8). This traverses all switching states to obtain the predicted state variables of $\boldsymbol{i}_1$, and $\boldsymbol{i}_2$ at instant $k+1$, respectively. Finally, the predicted and reference results are input to the cost function defined in (9), and the optimal switching sequence corresponding to the predicted value that minimizes the cost function is selected and directly acts on the *LCL*-GCCs as the control signals.

For the parameter identification and updating interrupt service routine, the filter parameter identification results are obtained by the RMSprop-GDO in (24), which periodically updates the filter parameters in the prediction model and the reference model. It is needed to note that *LCL* filter parameters are not changing very fast, it is unnecessary to update the model parameters in FCS-MPC controller at each control cycle. To solve this issue, in practice, the interrupt routine of parameter identification method with the proposed method should are set to be slower than the main predictive control loop. The parameter identification interrupt routine is executed only once when the FCS-MPC control program is executed four times.

D. Stability Analysis

The general description of the state-space mode considering model uncertainness is given as

$$\begin{cases} x(k+1) = Ax(k) + Bu(k) + Td(k) \\ \mathbf{y_c}(k) = \boldsymbol{\lambda_c} x(k) \end{cases} \tag{28}$$

where $\boldsymbol{x}(k) \in \mathbb{R}^{n_x}$ is the state variable, $\boldsymbol{u}(k) \in \mathbb{R}^{n_u}$ is the input control variable, $\boldsymbol{y_c}(k) \in \mathbb{R}^{n_c}$ is the output control variable. $\boldsymbol{d}(k)$ is the disturbance. Note that here grid voltage is seen as the disturbance.

To reduce the steady-state error, the system of (28) is rewritten as an increment model given by

$$\Delta \boldsymbol{x}(k+1) = \mathbf{A}\Delta \boldsymbol{x}(k) + \boldsymbol{B}\Delta \boldsymbol{u}(k) + \boldsymbol{T}\Delta \boldsymbol{d}(k) \tag{29}$$

where $\Delta x(k) = x(k) - x(k-1)$, $\Delta u(k) = u(k) - u(k-1)$, $\Delta d(k) = d(k) - d(k-1)$.

Since the prediction error of the system at instant $k+1$ can be given as

$$\begin{aligned} \boldsymbol{E}_P(k+1|k) &= \boldsymbol{R}(k+1) - \boldsymbol{Y}(k+1) \\ &= \boldsymbol{R}(k+1) - \boldsymbol{S}_x \Delta x(k) - \mathbf{y_c}(k) \\ &\quad - \boldsymbol{S_d}\Delta d(k) - \boldsymbol{S_u}\Delta \boldsymbol{u}(k) \end{aligned} \tag{30}$$

$$\begin{cases} i_1(k) = \frac{L_1(k)C_f(k)}{T_s^2 + R_C C_f(k) T_s + L_1(k) C_f(k)} i_1(\mathrm{k}-1) + \frac{T_s^2 + R_C C_f(k) T_S}{T_s^2 + R_C C_f(k) T_s + L_1(k) C_f(k)} i_2(k) + \frac{C_f(k) T_s}{T_s^2 + R_C C_f(k) T_s + L_1(k) C_f(k)} \\ \quad (0.5 V_{\mathrm{dc}} S_{abc}(k) - v_{\mathrm{c}}(k)) \\ v_c(k) = \frac{-L_2(k)}{T_s + R_C C_f(k)} i_2(\mathrm{k}-1) + \frac{R_C C_f(k)}{T_s + R_C C_f(k)} v_c(\mathrm{k}-1) + \frac{L_2(k)}{T_s + R_C C_f(k)} i_2(k) + \frac{T_s}{T_s + R_C C_f(k)} v_g(k) \end{cases} \tag{26}$$

Authorized licensed use limited to: Universidad Andres Bello. Downloaded on June 25,2024 at 19:34:06 UTC from IEEE Xplore. Restrictions apply.

where

$$\boldsymbol{S}_x = [\boldsymbol{\lambda A}\, \boldsymbol{\lambda A}^2 \boldsymbol{\lambda A}^3 \ldots \boldsymbol{\lambda A}^N]^T$$

$$\urcorner = [\boldsymbol{I}_{nc\times nc}\ \boldsymbol{I}_{nc\times nc}\ \ldots \boldsymbol{I}_{nc\times nc}]^T$$

$$\boldsymbol{S_d} = \begin{bmatrix} \boldsymbol{\lambda B} & 0 & \cdots & 0 \\ \boldsymbol{\lambda AB} & \boldsymbol{\lambda B} & \cdots & 0 \\ \vdots & \vdots & \ddots & \vdots \\ \boldsymbol{\lambda A}^{N-1}\boldsymbol{B} & \boldsymbol{\lambda A}^{N-2}\boldsymbol{B} & \cdots & \boldsymbol{\lambda B} \end{bmatrix}$$

$$\boldsymbol{S_u} = \begin{bmatrix} \boldsymbol{\lambda T} & 0 & \cdots & 0 \\ \boldsymbol{\lambda AT} & \boldsymbol{\lambda T} & \cdots & 0 \\ \vdots & \vdots & \ddots & \vdots \\ \boldsymbol{\lambda A}^{N-1}\boldsymbol{T} & \boldsymbol{\lambda A}^{N-2}\boldsymbol{T} & \cdots & \boldsymbol{\lambda T} \end{bmatrix}.$$

According to the operation principle of MPC, Only the first element of the open-loop optimal control sequence will act on the system, namely

$$\Delta \boldsymbol{u} = \left[\boldsymbol{I}_{nc\times nc}\ 0 \cdots 0\right] \Delta \boldsymbol{U}^*(k) \tag{31}$$

where $\Delta \boldsymbol{U}^*$ is the optimal control sequence given as

$$\Delta \boldsymbol{U}^*(k) = \left(S_u^T \Gamma_y^T \Gamma_y S_u + \Gamma_u^T \Gamma_u\right)^{-1} S_u^T \Gamma_y^T \boldsymbol{E}_P(k+1|k). \tag{32}$$

Defining the control gain $\boldsymbol{K}_{\mathrm{mpc}}$ of the prediction controller as

$$\boldsymbol{K}_{\mathrm{mpc}} = \left[\boldsymbol{I}_{nc\times nc}\ 0 \cdots 0\right]_{1\times m} \times \left(S_u^T \Gamma_y^T \Gamma_y S_u + \Gamma_u^T \Gamma_u\right)^{-1} S_u^T \Gamma_y^T \boldsymbol{E}_P(k+1|k). \tag{33}$$

Thus, $\Delta \boldsymbol{u}(k)$ can be derived by (32) and (33) as

$$\begin{aligned} \Delta \boldsymbol{u}(k) &= \boldsymbol{K}_{\mathrm{mpc}} \boldsymbol{E}_P(k+1|k) \\ &= \boldsymbol{K}_{\mathrm{mpc}}(\boldsymbol{R}(k+1) - \boldsymbol{S}_x \Delta \boldsymbol{x}(k) - \urcorner \boldsymbol{\lambda_c} \boldsymbol{x}(k) \\ &\quad - \boldsymbol{S_d} \Delta \boldsymbol{d}(k)\, \boldsymbol{K}_{\mathrm{mpc}} \boldsymbol{R}(k+1) \\ &\quad - \boldsymbol{K}_{\mathrm{mpc}}(\boldsymbol{S_x} + \urcorner \boldsymbol{\lambda_c})\, \Delta \boldsymbol{x}(k) - \boldsymbol{K}_{\mathrm{mpc}} \urcorner \boldsymbol{\lambda}_c x(k-1) \\ &\quad - \boldsymbol{K}_{\mathrm{mpc}} \boldsymbol{S}_d \Delta d(k). \end{aligned} \tag{34}$$

Thus, the closed-loop system can be written as

$$\begin{aligned} \Delta \boldsymbol{x}(k+1) = {} & (\boldsymbol{A} - \boldsymbol{B}\boldsymbol{K}_{\mathbf{mpc}}(\boldsymbol{S}_x + \urcorner \boldsymbol{\lambda}_c))\, \Delta \boldsymbol{x}(k) \\ & + \boldsymbol{B}\boldsymbol{K}_{\mathrm{mpc}} \boldsymbol{R}(k+1) + (\boldsymbol{T} - \boldsymbol{B} K_{\mathrm{mpc}} S_d)\, \Delta \boldsymbol{d}(k) \\ & - \boldsymbol{B} K_{\mathrm{mpc}} \urcorner \boldsymbol{\lambda}_c \boldsymbol{x}(k-1). \end{aligned} \tag{35}$$

Obviously, when all the characteristic roots of the matrix $\boldsymbol{A} - \boldsymbol{B}\boldsymbol{K}_{\mathrm{mpc}}(\boldsymbol{S_x} + \urcorner \boldsymbol{\lambda_c})$ are located with the unit circle, the closed-loop control system would be stable. For *LCL*-GCCs, $\boldsymbol{K}_{\mathrm{mpc}}$ is the optimal switching sequence that can minimize the cost function, which can guarantee $|\boldsymbol{A} - \boldsymbol{B}\boldsymbol{K}_{\mathrm{mpc}}(\boldsymbol{S_x} + \urcorner \boldsymbol{\lambda_c})| < 1$.

V. Experiment Results

A. Hardware Setup

To validate the correctness of the proposed method in utility, a hardware prototype of a 10-kVA three-phase two-level *LCL*-GCCs is setup in the laboratory. Fig. 6 shows the hardware configurations. Table I shows the experimental parameters. Three groups of the *LCL*-filter parameters are shown in Table II. The control scheme is implemented with a 32-bit float-point DSP TMS320F28335 from Texas Instruments, which has been widely used for complicated mathematics calculations and control algorithm implementation. The power converter is composed of six power transistors with the IMZ120R045M1 from Infineon company. All the power MOSFETs are driven by the isolation driver 1ED20I12FA2. Six Hall current sensors (HCS-LTS-06A) are used for inverter-side and grid-side current measurements.

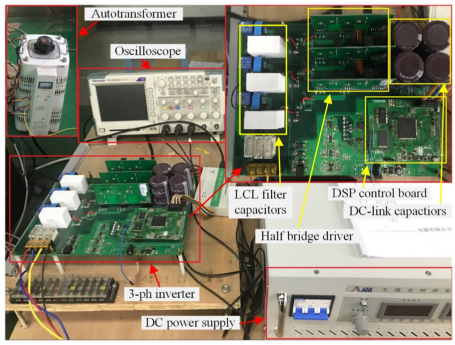


Fig. 6. Experimental configurations and designed *LCL*-GCC.

TABLE II
Different Filter Parameter Groups for Identification

Group	L_1	L_2	C_f
A	4.0 mH	2.0 mH	10.0 μF
B	4.6 mH	2.3 mH	11.5 μF
C	3.4 mH	1.7 mH	8.5 μF

For grid and filter capacitor voltage sampling, a high precision series voltage divider and a full differential isolation amplifier ACPL-C790 with 0.5% high gain accuracy, 0.05% excellent linearity, and 200-kHz wide-bandwidth are used. Since the output voltage ranges from −1.5 to 1.5 V, a forward-bias voltage circuit with a single-supply and rail-to-rail operational amplifier OPA4340 is used to convert −1.5–1.5 V into 0–3 V. This allows the system to connect with the ADC port of the microprocessor.

In program design for the microprocessor (TMS320F28335), the interrupt routine for normal FCS-MPC control of the *LCL*-GCCs takes about 20 μs, considering that the filter parameter does not change so rapidly comparing with the converter-side and grid-side currents, thus, the parameter estimation interrupt routine for RMSprop-GDO method is given by 100 μs. The modeling parameters in FCS-MPC are periodically updated by the identified results from RMSprop-GDO interrupt routine.

The learning rates are initialized as $\eta_1 = 5{\cdot}10^{-5}$, $\eta_2 = 5{\cdot}10^{-5}$, and $\eta_3 = 5{\cdot}10^{-3}$, respectively. The main parameter specifications of the system are listed in Table I.

To verify the effectiveness of the proposed parameter identification method under different scenarios, three sets of the filter parameters are provided in Table II.

The experiments are conducted for two main purposes: 1) validate the correctness and effectiveness of the proposed parameter identification method under steady-state, transient-response, distorted grid voltage, and grid impedance. 2) Evaluate the

Authorized licensed use limited to: Universidad Andres Bello. Downloaded on June 25,2024 at 19:34:06 UTC from IEEE Xplore. Restrictions apply.

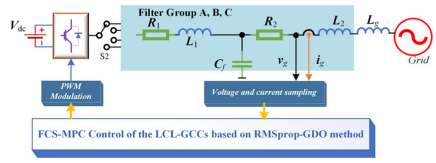


Fig. 7. Block diagram of the experimental *LCL*-GCCs with the RMSprop-GDO method.

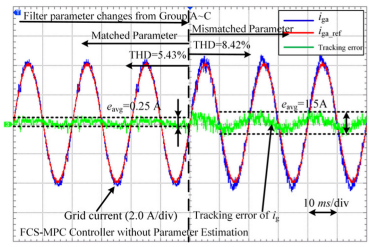


Fig. 8. Grid current under matched and mismatched filter parameters.

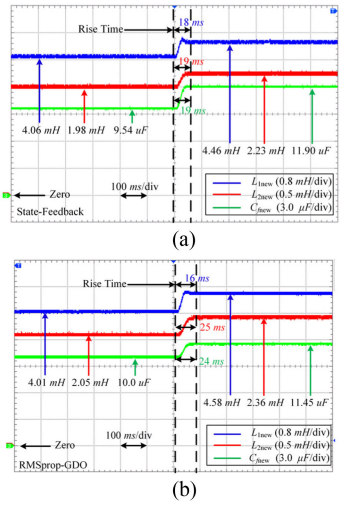


Fig. 9. Parameter identification comparisons of the *LCL*-filter changing from group A to B. (a) State-Feedback method. (b) RMSprop-GDO method.

control effect of the FCS-MPC for *LCL*-GCCs with the updated parameters.

Fig. 7 shows the implementation of the experimental *LCL*-GCCs under different scenarios, which is used to verify the performance of the proposed method under a step-up and step-down of the filter parameter changes (with the help of S2 to switch between different filter parameters). Performance of the proposed method under different grid impedance is also verified.

B. Results and Analysis

The experimental verification contains the following scenarios.

1) Power quality of the grid current under mismatched parameters with the FCS-MPC controller.
2) Parameter identification performance with the state-feedback method and the proposed RMSprop-GDO method under the step-up and step-down parameter variations.
3) Parameter identification results under distorted grid voltage.
4) Tracking performance and dynamic response of the grid current.
5) Parameter identification performance under grid impedance changes.

1) Tracking Error of the Grid Current Under Mismatched Parameters: Fig. 8 shows the waveforms of the grid current with mismatched filter parameters in FCS-MPC control, where no parameter observers are applied. The working filter parameters switch from Group A to C, which is used to emulate the influence of a temperature rise in utility. Note that the model parameters used in the FCS-MPC controller remains unchanged (still Group A), and as a result a parameter mismatch occurs between the working parameters and the model parameters. The green-line in Fig. 8 indicates that the average tracking error of the grid current raises from 0.25 to 1.5 A, and THD of the grid current increases from 5.43 to 8.42%.

2) Identification Performance of the Observer Under Filter Parameter Variations: Fig. 9 shows that the filter parameter identification results for when the step-up increase of *LCL*-filter parameters from Group A to B. Fig. 9(a) uses the conventional state-feedback parameter identification method, the dynamic time responses of state-feedback method for L_1, L_2, and C_f are about 18, 19, and 19 ms, respectively. After entering steady state, their average values are 4.46 mH, 2.23 mH, and 11.90 μF, respectively. The average steady-state errors are 3.04%, 3.04%, and 3.48%.

Fig. 9(b) shows the filter parameter identification results with RMSprop-GDO method, the dynamic response times for L_1, L_2, and C_f are 16, 25, and 24 ms, respectively. After entering steady state, their average values are 4.58 mH, 2.36 mH, and 11.45 μF, respectively. The average filter parameter estimation errors are 0.43%, 2.61%, and 0.43%, respectively. The proposed RMSprop-GDO method is superior to conventional state-feedback method when the step-up parameter variation occurs.

To verify the effectiveness of the proposed parameter identification method under a step-down parameter variation (Group A to C), the working parameters of the *LCL*-filter decrease from Group A to C. As shown in Fig. 10(a), for steady-state observer, the dynamic response time for L_1, L_2, and C_f are 16, 16, and 15 ms, respectively. Their average values are 3.36 mH, 1.64 mH, and 8.34 μF, respectively. The average observation errors are 1.18%, 3.53%, and 1.88%, respectively.

Fig. 10(b) shows the parameter observation results with RMSprop-GDO method. The observed results for L_1, L_2, and C_f are 47, 41, and 31 ms, respectively. Their average values are 3.42 mH, 1.73 mH, and 8.48 μF, respectively, and average observation errors are 0.59%, 1.76%, and 0.24%, respectively. Thus, comparing (a) with (b) in Fig. 9, the filter parameter observation errors are improved by 0.5882%, 1.7647%, and 1.6471%, respectively. The RMSprop-GDO method is superior to state-feedback method in this case.

Authorized licensed use limited to: Universidad Andres Bello. Downloaded on June 25,2024 at 19:34:06 UTC from IEEE Xplore. Restrictions apply.

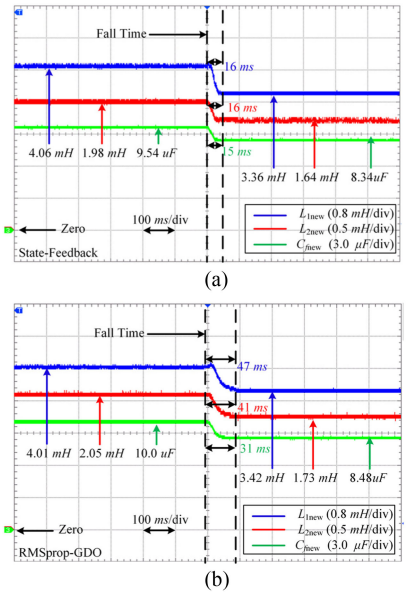


Fig. 10. Parameter identification comparisons of the *LCL*-filter changing from group A to C. (a) State-feedback method. (b) RMSprop-GDO method.

3) Parameter Identification Under Grid Voltage Distortions: To verify the robustness of the parameter identification method under distorted grid voltage, the fifth-order harmonics with 0.1 times amplitude of the fundamental frequency are superposed in the grid voltage. Fig. 11(a) shows the waveform of the distorted grid voltage and current. The parameter identification results when the filter parameters switch from Group-A to B are shown in Fig. 11(b) and (c). Fig. 11(b) shows that the dynamic response times of parameter identification for L_1, L_2, and C_f are 18, 19, and 19 ms, respectively. After entering steady state, their average values are 4.46 mH, 2.24 mH, and 11.90 μF, and the average steady-state errors of the *LCL*-filter are 3.04%, 2.60%, and 3.48%, respectively. Fig. 11(c) shows that the dynamic response times for L_1, L_2, and C_f are 18, 19, and 21 ms, respectively. After entering steady state, their average values are 4.56 mH, 2.36 mH, and 11.46 μF, respectively and average steady-state errors are 0.87%, 2.61%, and 0.35%, respectively. The observation errors are improved by 2.17%, 0.01%, and 3.13%.

The results in Fig. 11(b) and (c) indicate that the parameter identification results of two methods are hardly influenced by the distorted grid voltage, including dynamic response times and identification accuracy. Comparing to the state-feedback method, the RMSprop-GDO method has higher parameter identification accuracy.

4) Tracking Performance of the Grid Current: Fig. 12 shows the waveforms of the grid current without and with parameter observer, where the actual filter parameters are Group-C while the modeling parameters in FCS-MPC controller are Group-A. Fig. 12(a) and (b) shows that the average tracking error e_{avg} with state-feedback and RMSprop-GDO methods are 0.5 and 0.25 A, respectively. The steady-state tracking error of the grid current is reduced by 0.25 A. Fig. 12(c) and (d) indicates that the THD of the grid current with state-feedback and RMSprop-GDO method decreases from 7.05 to 6.24%. Therefore, power quality of the grid current is enhanced by 0.81%.

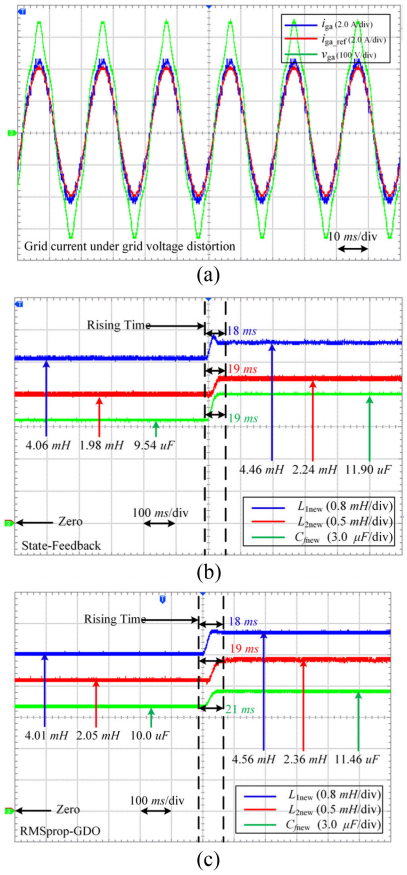


Fig. 11. Filter parameter identification comparisons under distorted grid voltage. (a) Distorted grid voltage and grid current. (b) State-feedback method. (b) RMSprop-GDO method.

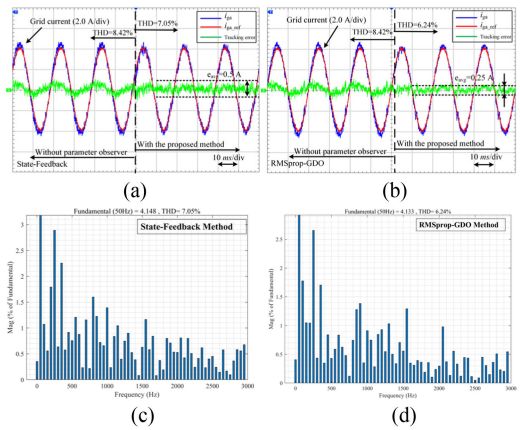


Fig. 12. Tracking performance and THD of the grid current. (a) State-feedback method. (b) RMSprop-GDO method. (c) THD of (a). (d) THD of (b).

5) Dynamic Response of the Grid Current: Fig. 13 demonstrates the dynamic response of the grid current with RMSprop-GDO and state-feedback methods, where the filter

Authorized licensed use limited to: Universidad Andres Bello. Downloaded on June 25,2024 at 19:34:06 UTC from IEEE Xplore. Restrictions apply.

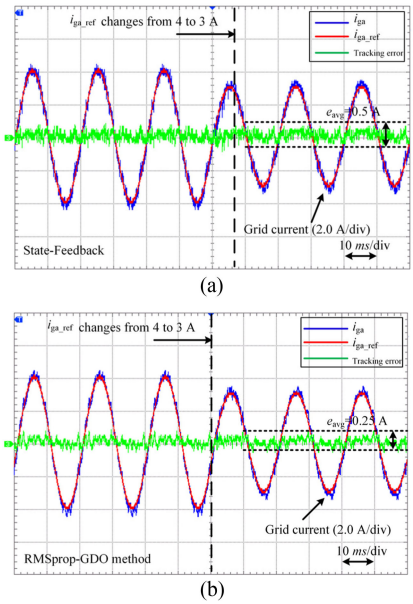


Fig. 13. Dynamic response of the grid current. (a) State-feedback method. (b) RMSprop-GDO method.

parameters change from Group A to C and a step-down grid current reference is given from 4 to 3 A. The results indicate that the grid current can be well tracked. Both RMSprop-GDO and state-feedback methods could achieve very good dynamic response. After re-entering steady state, the tracking error with proposed observer [see Fig. 13(b)] is 0.25 A, compared to 0.5 A with state-feedback observer [see Fig. 13(a)]. This demonstrates that the proposed method could maintain good dynamic response as well as smaller tracking errors.

6) Parameter Identification Considering Grid Impedance: Fig. 14 shows the parameter identification results and tracking control of the grid current when the grid impedance increases from 0 to 3 mH. As shown in Fig. 14(a), the *LCL*-filter parameter identification results for group-C are almost uninfluenced. Fig. 14(b) and (c) shows the waveforms of the grid current considering grid impedance, where the grid inductance increases from 0 to 3 mH. The results show that the tracking errors of the grid current are reduced with the increase of grid impedance. Tracking performance of the grid current with the two methods are very close. The filter parameter identification results will not be influenced. As a result, the system stability still can be guaranteed.

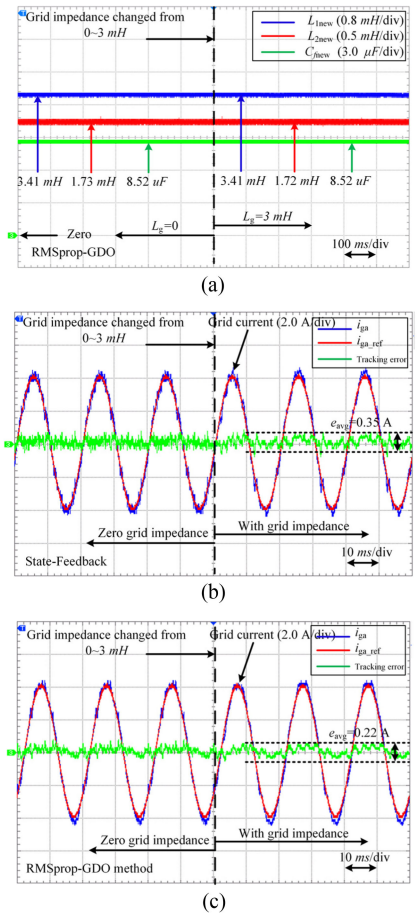


Fig. 14. Parameter identification results under grid impedance changes. (a) Parameter identification results. (b) State-feedback method. (c) RMSprop-GDO method.

VI. Conclusion

This article investigated an online parameter identification method based on RMSprop-GDO for *LCL*-GCCs, comparing to the state-feedback parameter identification method, the proposed method has higher identification accuracy. The proposed method appears to provide an objective function, defined as the filter parameter estimation error between the actual and estimated values, which is minimized by searching for the optimal iteration step-size along the gradient direction of the parameter matrix. The optimal iteration step size with the RMSprop-GDO method was proposed to achieve fast and high accuracy parameter estimation. The model parameters in the FCS-MPC controller were updated periodically by the observed parameters. The experimental results showed that the proposed parameter identification method can quickly track the actual filter parameters in both steady state and transient state under parameter mismatches. Thereby the power quality and tracking control of the grid current can be significantly improved when RMSprop-GDO method was applied. It is suggested that future research can be focused on applying this method to FCS-MPC controlled ac motor drive system.

References

[1] K. Nishida, T. Ahmed, and M. Nakaoka, "A novel finite-time settling control algorithm designed for grid-connected three-phase inverter with an LCL-Type filter," *IEEE Trans. Ind. Appl.*, vol. 50, no. 3, pp. 2005–2020, May/Jun. 2014.

[2] B. Liu, Q. Wei, C. Zou, and S. Duan, "Stability analysis of LCL-Type grid-connected inverter under single-loop inverter-side current control with capacitor voltage feedforward," *IEEE Trans. Ind. Informat.*, vol. 14, no. 2, pp. 691–702, Feb. 2018.

[3] W. Wu, Y. Liu, Y. He, H. S. Chung, M. Liserre, and F. Blaabjerg, "Damping methods for resonances caused by LCL-Filter-Based current-controlled grid-tied power inverters: An overview," *IEEE Trans. Ind. Electron.*, vol. 64, no. 9, pp. 7402–7413, Sep. 2017.

Authorized licensed use limited to: Universidad Andres Bello. Downloaded on June 25,2024 at 19:34:06 UTC from IEEE Xplore. Restrictions apply.

[4] Y. Liu, W. Wu, Y. He, Z. Lin, F. Blaabjerg, and H. S. Chung, "An efficient and robust hybrid damper for LCL- or LLCL-Based grid-tied inverter with strong grid-side harmonic voltage effect rejection," *IEEE Trans. Ind. Electron.,* vol. 63, no. 2, pp. 926–936, Feb. 2016.

[5] R. P. Vieira, L. T. Martins, J. R. Massing, and M. Stefanello, "Sliding mode controller in a multiloop framework for a grid-connected VSI with LCL filter," *IEEE Trans. Ind. Electron.,* vol. 65, no. 6, pp. 4714–4723, Jun. 2018.

[6] X. Mu, J. Wang, W. Wu, and F. Blaabjerg, "A modified multifrequency passivity-based control for shunt active power filter with model-parameter-adaptive capability," *IEEE Trans. Ind. Electron.,* vol. 65, no. 1, pp. 760–769, Jan. 2018.

[7] F. Lin, K. Lu, T. Ke, B. Yang, and Y. Chang, "Reactive power control of three-phase grid-connected PV system during grid faults using Takagi–Sugeno–Kang probabilistic fuzzy neural network control," *IEEE Trans. Ind. Electron.,* vol. 62, no. 9, pp. 5516–5528, Sep. 2015.

[8] S. Li, M. Fairbank, C. Johnson, D. C. Wunsch, E. Alonso, and J. L. Proao, "Artificial neural networks for control of a grid-connected rectifier/inverter under disturbance, dynamic and power converter switching conditions," *IEEE Trans. Neural Netw. Learn. Syst.,* vol. 25, no. 4, pp. 738–750, Apr. 2014.

[9] S. Zhao, F. Blaabjerg, and H. Wang, "An overview of artificial intelligence applications for power electronics," *IEEE Trans. Power Electron.,* vol. 36, no. 4, pp. 4633–4658, Apr. 2021.

[10] X. Fu and S. Li, "Control of single-phase grid-connected converters with LCL filters using recurrent neural network and conventional control methods," *IEEE Trans. Power Electron.,* vol. 31, no. 7, pp. 5354–5364, Jul. 2016.

[11] S. Yang, Q. Lei, F. Z. Peng, and Z. Qian, "A robust control scheme for grid-connected voltage-source inverters," *IEEE Trans. Ind. Electron.,* vol. 58, no. 1, pp. 202–212, Jan. 2011.

[12] P. Karamanakos, E. Liegmann, T. Geyer, and R. Kennel, "Model predictive control of power electronic systems: Methods, results, and challenges," *IEEE Open J. Ind. Appl.,* vol. 1, pp. 95–114, Aug. 2020.

[13] M. Rivera, J. Rodriguez, and S. Vazquez, "Predictive control in power converters and electrical drives—Part III," *IEEE Trans. Ind. Electron.,* vol. 63, no. 8, pp. 5130–5132, Aug. 2016.

[14] M. Rivera, J. Rodriguez, and S. Vazquez, "Predictive control in power converters and electrical drives—Part ii [guest Ed.ial]," *IEEE Trans. Ind. Electron.*, vol. 63, no. 7, pp. 4472–4474, Jul. 2016.

[15] M. Rivera, J. Rodriguez, and S. Vazquez, "Predictive control in power converters and electrical drives—Part I," *IEEE Trans. Ind. Electron.,* vol. 63, no. 6, pp. 3834–3836, Jun. 2016.

[16] S. Vazquez *et al.*, "Model predictive control: A review of its applications in power electronics," *IEEE Ind. Electron. Mag.,* vol. 8, no. 1, pp. 16–31, Mar. 2014.

[17] M. Narimani, W. Bin, V. Yaramasu, C. Zhongyuan, and N. R. Zargari, "Finite control-set model predictive control (FCS-MPC) of nested neutral point-clamped (NNPC) converter," *IEEE Trans. Power Electron.,* vol. 30, no. 12, pp. 7262–7269, Dec. 2015.

[18] M. Novak, U. M. Nyman, T. Dragicevic, and F. Blaabjerg, "Analytical design and performance validation of finite set MPC regulated power converters," *IEEE Trans. Ind. Electron.,* vol. 66, no. 3, pp. 2004–2014, Mar. 2019.

[19] M. Siami, D. A. Khaburi, M. Rivera, and J. Rodríguez, "A computationally efficient lookup table based FCS-MPC for PMSM drives fed by matrix converters," *IEEE Trans. Ind. Electron.,* vol. 64, no. 10, pp. 7645–7654, Oct. 2017.

[20] S. C. Ferreira, R. B. Gonzatti, R. R. Pereira, C. H. d. Silva, L. E. B. d. Silva, and G. Lambert-Torres, "Finite control set model predictive control for dynamic reactive power compensation with hybrid active power filters," *IEEE Trans. Ind. Electron.,* vol. 65, no. 3, pp. 2608–2617, Mar. 2018.

[21] H. A. Young, V. A. Marin, C. Pesce, and J. Rodriguez, "Simple finite-control-set model predictive control of grid-forming inverters with LCL filters," *IEEE Access,* vol. 8, pp. 81246–81256, 2020.

[22] Y. B. Zbede, S. M. Gadoue, and D. J. Atkinson, "Model predictive MRAS estimator for sensorless induction motor drives," *IEEE Trans. Ind. Electron.,* vol. 63, no. 6, pp. 3511–3521, Jun. 2016.

[23] J. Yin, S. Duan, and B. Liu, "Stability analysis of grid-connected inverter with LCL filter adopting a digital single-loop controller with inherent damping characteristic," *IEEE Trans. Ind. Informat.,* vol. 9, no. 2, pp. 1104–1112, May 2013.

[24] T. Wu, M. Misra, L. Lin, and C. Hsu, "An improved resonant frequency based systematic LCL filter design method for grid-connected inverter," *IEEE Trans. Ind. Electron.,* vol. 64, no. 8, pp. 6412–6421, Aug. 2017.

[25] M. Lu, A. Al-Durra, S. M. Muyeen, S. Leng, P. C. Loh, and F. Blaabjerg, "Benchmarking of stability and robustness against grid impedance variation for LCL -Filtered grid-interfacing inverters," *IEEE Trans. Power Electron.,* vol. 33, no. 10, pp. 9033–9046, 2018, doi: 10.1109/TPEL.2017.2784685.

[26] M. A. Perez, J. Rodriguez, E. J. Fuentes, and F. Kammerer, "Predictive control of AC–AC modular multilevel converters," *IEEE Trans. Ind. Electron.,* vol. 59, no. 7, pp. 2832–2839, Jul. 2012.

[27] H. A. Young, M. A. Perez, and J. Rodriguez, "Analysis of finite-control-set model predictive current control with model parameter mismatch in a three-phase inverter," *IEEE Trans. Ind. Electron.,* vol. 63, no. 5, pp. 3100–3107, May 2016.

[28] Y. Yang, S. Tan, and S. Y. R. Hui, "Adaptive reference model predictive control with improved performance for voltage-source inverters," *IEEE Trans. Control Syst. Technol.,* vol. 26, no. 2, pp. 724–731, Mar. 2018.

[29] J. M. Espi, J. Castello, R. García-Gil, G. Garcera, and E. Figueres, "An adaptive robust predictive current control for three-phase grid-connected inverters," *IEEE Trans. Ind. Electron.,* vol. 58, no. 8, pp. 3537–3546, Aug. 2011.

[30] J. R. Fischer, S. A. González, I. Carugati, M. A. Herrán, M. G. Judewicz, and D. O. Carrica, "Robust predictive control of grid-tied converters based on direct power control," *IEEE Trans. Power Electron.,* vol. 29, no. 10, pp. 5634–5643, Oct. 2014.

[31] H. Mohomad, S. A. Saleh, and L. Chang, "Disturbance estimator-based predictive current controller for single-phase interconnected PV systems," *IEEE Trans. Ind. Appl.,* vol. 53, no. 5, pp. 4201–4209, Sep. /Oct. 2017.

[32] Y. Lai, C. Lin, F. Chuang, and J. Yu, "Model-free predictive current control for three-phase AC/DC converters," *IET Electric Power Appl.,* vol. 11, pp. 729–739, 2017.

[33] C. Lin, T. Liu, J. Yu, L. Fu, and C. Hsiao, "Model-Free predictive current control for interior permanent-magnet synchronous motor drives based on current difference detection technique," *IEEE Trans. Ind. Electron.,* vol. 61, no. 2, pp. 667–681, Feb. 2014.

[34] P. G. Ipoum-Ngome, D. L. Mon-Nzongo, J. Song-Manguelle, R. C. C. Flesch, J. Tang, and T. Jin, "Model-Free predictive current control of a multilevel cascaded H-bridge inverter for photovoltaic systems," in *Proc. IEEE 13th Int. Conf. Power Electron. Drive Syst.*, 2019, pp. 1–6.

[35] S. Kwak, U. Moon, and J. Park, "Predictive-Control-Based direct power control with an adaptive parameter identification technique for improved AFE performance," *IEEE Trans. Power Electron.,* vol. 29, no. 11, pp. 6178–6187, Nov. 2014.

[36] P. Antoniewicz and M. P. Kazmierkowski, "Virtual-Flux-Based predictive direct power control of AC/DC converters with online inductance estimation," *IEEE Trans. Ind. Electron.,* vol. 55, no. 12, pp. 4381–4390, Dec. 2008.

[37] V. Pirsto, J. Kukkola, F. M. M. Rahman, and M. Hinkkanen, "Real-Time identification of LCL filters employed with grid converters," *IEEE Trans. Ind. Appl.,* vol. 56, no. 5, pp. 5158–5169, Sep./Oct. 2020.

[38] S. Mao, W. Liu, N. Jiao, G. Luo, Y. Jiang, and Y. Hu, "Design and implementation of parameter estimation and start control of brushless synchronous starter/generators under sudden excitation change," *IEEE Trans. Ind. Electron.,* vol. 67, no. 5, pp. 3551–3561, May 2020.

[39] L. H. Wang, G. J. Tan, and J. Meng, "Research on model predictive control of IPMSM based on adaline neural network parameter identification," *Energies,* vol. 12, p. 4803, Dec. 17, 2019, doi: 10.3390/en12244803.

[40] J. Scoltock, T. Geyer, and U. K. Madawala, "Model predictive direct power control for grid-connected NPC converters," *IEEE Trans. Ind. Electron.,* vol. 62, no. 9, pp. 5319–5328, Sep. 2015.

[41] X. Liu, D. Wang, and Z. H. Peng, "Improved finite-control-set model predictive control for active front-end rectifiers with simplified computational approach and on-line parameter identification," *ISA Trans.,* vol. 69, pp. 51–64, Jul 2017.

[42] B. Long, T. Cao, W. T. Fang, T. C. Kil, and J. M. Guerrero, "Model predictive control of a three-phase two-level four-leg grid-connected converter based on sphere decoding method," *IEEE Trans. Power Electron.,* vol. 36, no. 2, pp. 2283–2297, Feb. 2021.

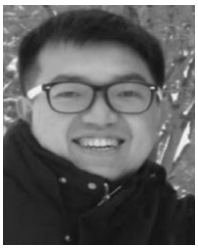
[43] V. Yaramasu, M. Rivera, B. Wu, and J. Rodriguez, "Model predictive current control of two-level four-leg inverters—Part I: Concept, algorithm, and simulation analysis," *IEEE Trans. Power Electron.,* vol. 28, no. 7, pp. 3459–3468, Jul. 2013.

[44] F. X. Wang, H. T. Xie, Q. Chen, S. A. Davari, J. Rodriguez, and R. Kennel, "Parallel predictive torque control for induction machines without weighting factors," *IEEE Trans. Power Electron.,* vol. 35, no. 2, pp. 1779–1788, Feb. 2020.

Authorized licensed use limited to: Universidad Andres Bello. Downloaded on June 25,2024 at 19:34:06 UTC from IEEE Xplore. Restrictions apply.

[45] S. Kwak, U. C. Moon, and J. C. Park, "Predictive-control-based direct power control with an adaptive parameter identification technique for improved AFE performance," *IEEE Trans. Power Electron.,* vol. 29, no. 11, pp. 6178–6187, Nov. 2014.

[46] B. Wang, Y. Xu, Z. Shen, J. Zou, C. Li, and H. Liu, "Current control of grid-connected inverter with LCL filter based on extended-state observer estimations using single sensor and achieving improved robust observation dynamics," *IEEE Trans. Ind. Electron.,* vol. 64, no. 7, pp. 5428–5439, Jul. 2017.



Bo Long (Member, IEEE) received the B.S. degree from the Xi'an Petroleum University, Xi'an, China, in 2001, and the Ph.D. degree from Xian Jiaotong University, Shanxi, China, in 2008, both in electrical engineering.

He was with the Department of Power Electronics, School of Mechatronics Engineering, University of Electronic Science and Technology of China, in 2008, and has been promoted to an Associate Professor since 2014. From 2017 to 2018, he was a Visiting Scholar (Guest Postdoctoral Researcher) in the area of renewable energy and microgrids with the Department of Electrical Engineering, Tsinghua University, Beijing, China. He is currently the supervisor for eleven master students, two of which have been nominated as provincial outstanding graduate student of UESTC. He has authored more than 20 SCIE-indexed journal papers and one book chapter in the area of power electronics, motor control, battery management system, and smart grid. He has seven issued and ten pending patents. His research interests include ac/dc microgrids, grid-connected converters for renewable energy systems and DGs, model predictive control, power quality, multilevel converters, ac motor control, and resonance suppression technique for smart grid applications.

Prof. Long is an Active Reviewer for the IEEE TRANSACTIONS ON POWER ELECTRONICS, ISA Transactions, Applied Energy, Energy, IEEE TRANSACTIONS ON SMART GRID, IEEE TRANSACTIONS ON INDUSTRIAL ELECTRONICS, IEEE TRANSACTIONS ON SUSTAINABLE ENERGY, and IEEE TRANSACTIONS ON ENERGY CONVERSION.



Zilin Zhu received the B.S. degree in mechanical engineering from the College of Mechanical and Electrical Engineering, Shaanxi University of Science and Technology, Xi'an, China, in 2017. He is currently working toward the M.S. degree in mechanical engineering from the University of Electronic Science and Technology of China, Chengdu, China.

His current research interests include the Finite control set-model predictive control, filter parameter identification of grid-connected inverter.



Wandi Yang is currently working toward the B.S. degree from Glasgow College, University of Electronic Science and Technology of China, Chengdu, China, where she has the qualification to study for a master's degree in mechanical engineering.

She is currently working on the adaptive parameter identification techniques for LCL-type grid connected converters.



Kil To Chong received the Ph.D. degree in mechanical engineering from Texas A&M University, College Station, TX, USA, in 1995.

He is currently a Professor and the Department Head with the School of Electronics and Information Engineering and a member and the Head of the Advanced Electronics and Information Research Center, Chonbuk National University, Jeonju, South Korea. His research interests include motor fault detection and control, network system control, sensor network systems, time-delay systems, and neural networks.



José Rodríguez (Fellow, IEEE) received the Engineer degree from the Universidad Tecnica Federico Santa Maria, Valparaiso, Chile, in 1977 and the Dr.-Ing. degree from the University of Erlangen, Erlangen, Germany, in 1985, both in electrical engineering.

He has been with the Department of Electronics Engineering, Universidad Tecnica Federico Santa Maria, since 1977, where he was a Full Professor and President. Since 2015, he has been the President of Universidad Andres Bello in Santiago, Chile. He has coauthored two books, several book chapters, and more than 400 journal and conference papers. His main research interests include multilevel inverters, new converter topologies, control of power converters, and adjustable-speed drives.

Prof. Rodríguez was the recipient of a number of best paper awards from journals of the IEEE. He is a member of the Chilean Academy of Engineering. In 2014, he received the National Award of Applied Sciences and Technology from the government of Chile. In 2015, he received the Eugene Mittelmann Award from the Industrial Electronics Society of the IEEE.



Josep M. Guerrero (Fellow, IEEE) received the B.S. degree in telecommunications engineering, the M.S. degree in electronics engineering, and the Ph.D. degree in power electronics from the Technical University of Catalonia, Barcelona, Spain, in 1997, 2000, and 2003, respectively.

Since 2011, he has been a Full Professor with the Department of Energy Technology, Aalborg University, Denmark, where he is responsible for the Microgrid Research Program. From 2014, he is the Chair Professor with Shandong University; from 2015, he is a Distinguished Guest Professor with Hunan University; and from 2016, he is a Visiting Professor Fellow with Aston University, U.K., and a Guest Professor with the Nanjing University of Posts and Telecommunications. From 2019, he was a Villum Investigator by The Villum Fonden, which supports the Center for Research on Microgrids, Aalborg University, he is the Founder and Director of the same center. He has authored and coauthored more than 600 journal papers in the fields of microgrids and renewable energy systems, which are cited more than 50000 times. His research interests include different microgrid aspects, including power electronics, distributed energy-storage systems, hierarchical and cooperative control, energy management systems, smart metering, the Internet of Things for ac–dc microgrid clusters and islanded microgrids, and specially focused on microgrid technologies applied to offshore wind, maritime microgrids for electrical ships, vessels, ferries and seaports, and space microgrids applied to nanosatellites and spacecrafts.

Prof. Guerrero is an Associate Editor for a number of IEEE Transactions. He was the recipient of the best paper award of the IEEE TRANSACTIONS ON ENERGY CONVERSION for the period 2014-2015, and the best paper prize of IEEE-PES in 2015. As well, he received the best paper award of the Journal of Power Electronics in 2016. During six consecutive years, from 2014 to 2019, he was awarded by Clarivate Analytics (former Thomson Reuters) as Highly Cited Researcher with 50 highly cited papers. In 2015, he was elevated as IEEE Fellow for his contributions on "distributed power systems and microgrids."

Authorized licensed use limited to: Universidad Andres Bello. Downloaded on June 25,2024 at 19:34:06 UTC from IEEE Xplore. Restrictions apply.